Larger seems twistier : Spectral Analysis of Gyrification patterns (SpAnGy) applied to adult brain size polymorphism

David Germanaud, Julien Lefèvre, Roberto Toro, Clara Fischer, Jessica Dubois, Lucie Hertz-Pannier, Jean-François Mangin

Larger seems twistier : Spectral Analysis of Gyrification patterns (SpAnGy) applied to adult brain size polymorphism.

David Germanaud[a,b,1,*], Julien Lefèvre[c,d,1,*], Roberto Toro[e], Clara Fischer[f], Jessica Dubois[g], Lucie Hertz-Pannier[a,b], Jean-Francois Mangin[f]

[a] *UMR 663, INSERM*
[b] *CEA, DSV, I2BM, Neurospin, LBIOM*
[c] *Aix-Marseille Univ, Département d'Informatique, Marseille, France*
[d] *CNRS, LSIS, UMR 6168, Marseille, France*
[e] *Institut Pasteur*
[f] *CEA, DSV, I2BM, Neurospin, LNAO*
[g] *CEA, DSV, I2BM, Neurospin, LCOGN*

Abstract

Keywords:

1. Introduction

The description of human cortical folding remains a major challenge for neuroimaging due to its great complexity and variability. On the one hand, a better knowledge of cortical folding would allow us to device more precise methods for inter-individual comparisons, on the other one, cortical folding is interesting in itself as research reveals subtle correlations with typical and pathological functioning (Fischl et al., 2007; Cachia et al., 2008). Sulci have been traditionally classified from a developmental point of view into primary, secondary and tertiary (Chi et al., 1977) according to their order of appearance during fetal life and early childhood. But cortical folding is probably a more continuous process than suggested by this classification (Armstrong et al., 1995), and successive folding phases may impact on each other (**?**) [PAUS, 1995, DON'T FIND THE ARTICLE] in a way that morphological features resulting from different phases can intricate into the same given fold. This interaction leads to a geometric complexity well described for the central

*These authors contributed equally to this work

Email addresses: david197@free.fr (David Germanaud), julien.lefevre@univmed.fr (Julien Lefèvre), rto@pasteur.fr (Roberto Toro), clara.fischer@cea.fr (Clara Fischer), jessica.dubois@cea.fr (Jessica Dubois), lucie.hertz-pannier@cea.fr (Lucie Hertz-Pannier), jean-francois.mangin@cea.fr (Jean-Francois Mangin)

[1]Corresponding authors

sulcus (White et al., 1997): sulci are not straight objects but show ramifications, digitations, nodes, dimples, etc. This complexity is associated with an important inter-individual variability (Yousry et al., 1997; Régis et al., 2005) which complicates the construction of folding atlases, even at a large-scale level. Eventually, as soon as mature gyrification is achieved, it is very difficult to attribute, based on morphological features alone, a primary, secondary or tertiary character to a given piece of a cortical fold (Fig. 1).

In the general population, human brain size is also highly variable, with the largest adult brains having up to 2 times the volume of the smallest ones (?Whitwell et al., 2001) [MILNER, 1990, DON'T FIND THE ARTICLE]. As for many biological objects, the relationship between cortical surface geometry (shape) and brain volume (size) is not simply homothetic: there are shape modifications coming with size variations (allometry). Across mammals, cortical surface area appears to scale proportionally with brain volume, whereas an isometric relationship would predict a scaling exponent of 2/3 (Prothero and Sundsten, 1984). A similar allometric scaling can be observed among humans, with scaling exponents in the order of 0.8 to 0.9 (Im et al., 2008; Toro et al., 2008). Indeed, large brains show a relative excess of cortical surface, which is accommodated by an increased folding. Several gyrification indexes have been proposed at hemispheric (Zilles et al., 1988) or local level (Schaer et al., 2008; Toro et al., 2008). They measure the proportion of cortical surface buried by folding, but are unable to distinguish an increase in the depth of the folds from an increase in the number of folds or in ramification. Such a modification of the complexity of cortical folding pattern (CFP) with brain size is nonetheless suspected: larger brains seem twistier (Fig. 1b). So far, attempts to propose a more descriptive assessment of gyrification complexity have provided rather preliminary results and there is no consensual measure, even at hemispheric level (Luders et al., 2004; Yotter et al., 2011). From a theoretical perspective, several models suggest that folding in an expanding domain should lead to the development of branching with doubling of the spatial frequency patterns (Fig. 1a). This phenomenon is observed with reaction-diffusion (Crampin et al., 1999; Striegel and Hurdal, 2009) and mechanical models (Mora and Boudaoud, 2006), but also with fractal approaches (Thompson et al., 1996; Yotter et al., 2011),. Thus, the study of the spatial frequencies of CFP should provide us an interesting new measure of gyrification complexity.

The grey/white matter interface of a brain hemisphere can be viewed as a closed surface of zero-genus (Dale et al., 1999) on which it is possible

to map scalar functions estimating surface characteristics such as curvature or sulcal depth. Theses oscillatory functions can be seen as proxies of the hemispheres gyrification pattern. The properties of CFP could then be studied through the analysis of its spatial oscillation frequencies. This spectral approach could be used to produce a power spectrum representative of the spatial frequencies composition of a cortical surface. The study of the eigenfunctions of the Laplace-Beltrami Operator (LBO) provides a natural method to obtain spectral decompositions of surfaces or, more generally, Riemannian manifolds (Berger, 2003). The methods necessary to apply this mathematical theory to the analysis of discrete meshes have been recently described by (Reuter et al., 2006) and (Lévy, 2006). One interest of this approach compared with the more traditional spherical harmonics decomposition is that it can be directly used with native data, without the non-linear alignment and spherical parametrization steps required by spherical harmonics decompositions (Chung et al., 2008; Hübsch and Tittgemeyer, 2008). Since folding wavelengths in the native surface are often projected onto the sphere with a different wavelength, such a parametrization necessarily induce a certain level of distance or angular distortions (Gu et al., 2004; Kruggel, 2008). In return, LBO-based spectral analysis requires to device an appropriate strategy to compare individually defined decompositions (Knossow et al., 2009).

In this article, we propose an original method for the Spectral Analysis of Gyrification (Spangy) which produces a morphologically relevant band power spectrum of CFP. We also report on the interest of Spangy for the study of the variability of CFP complexity with brain size in the comprehensive cohort of young healthy adults of the ICBM MRI database (Mazziotta et al., 1995; Watkins et al., 2001). Firstly, we present theoretical and numerical aspects of the LBO-based analysis, along with relevant Spangy design choices such as definition of curvature function, spectral bands or spectral segmentation of CFP. Next, we derive the measuring and describing properties of Spangy from our numerical and anatomical results in the ICBM database. Finally, we establish the relationship between spectral composition of CFP and brain size through allometric scaling. In the field of cortical surface study, LBO-based spectral analysis has been previously used only as a tool for surface smoothing (Vallet and Lévy, 2008). To our knowledge, this is the first time that this approach is used to provide a relevant signature of CFP and assess gyrification complexity.

2. Materials and Methods

2.1. Population

2.2. Subjects

We analyzed the 152 normal volunteers of the ICBM MRI database (Watkins et al., 2001). Each subject had a T1-weighted scan (3D fast field echo images, 140 to 160 slices, 1 mm isotropic resolution, TR = 18 ms, TE = 10 ms, flip angle = 30, Phillips Gyroscan 1.5T scanner). One scan was excluded because of its lesser quality, leading to artifacts in the automatic segmentation step. Of the remaining 151 subjects, 86 were males and 65 were females. Ages ranged from 18 to 44 years (mean age: 25 years, standard deviation: 4.9 years). 128 subjects were right-handed, 14 were left-handed, and handedness was unknown for the remaining 10.

2.3. Brain segmentation and morphometric parameters

T1-weighted images were automatically segmented with BrainVISA T1 segmentation pipeline (BrainVisa Software) to obtain topologically spherical mesh reconstructions of the left hemispheric hull (morphological closing of the hemispheric mask) and grey-white interface. The reconstructions were visually inspected for segmental disruption or excess of surface spicules, leading to the exclusion of one subject. The hemispheric volume (HV) i.e. the volume inside the hemispheric hull and the hemispheric surface area (HA) i.e. the area of the grey-white interface were computed for each left hemisphere using the BrainVISA Morphometry toolbox. The mean curvature of the grey-white interface (H) was computed using the non-parametric estimator implemented in the BrainVISA Surface toolbox, which is based on the method introduced by (Desbrun et al., 1999).

2.4. Laplace-Beltrami operator and spectral theory

Given a compact Riemannian manifold $(\mathcal{M}, g)$, where g is a metric tensor, we introduce $L^2(\mathcal{M}) = \{u : \mathcal{M} \to \mathbb{R} \,/\, \int_{\mathcal{M}} u^2 < +\infty\}$ and the scalar product $< u, v >= \int_{\mathcal{M}} uv$. The spectrum of the *Laplace-Beltrami operator* (LBO) $\Delta_{\mathcal{M}} = \mathrm{div} \circ \nabla_{\mathcal{M}}$ is discrete (Berger, 2003). We denote $\lambda_0 = 0 \leq \lambda_1 \leq ...$ the *eigenvalues* of $-\Delta_{\mathcal{M}}$ and $\phi_0, \phi_1, ...$ an associated orthonormal basis of eigenfunctions in $L^2(\mathcal{M})$ that satisfy:

$$-\Delta_{\mathcal{M}} \phi_n = \lambda_n \phi_n. \tag{1}$$

Given an eigenfunction ϕ_n, the nodal set of ϕ_n is defined as $\{x \in \mathcal{M}, \phi_n(x) = 0\}$. The connected components of the complement of the nodal set are called *nodal domains*. The Courant Nodal Domain Theorem ensures that if ϕ_n is not the first eigenfunction, the number of nodal domains is at least 2 and at most n. Moreover any function $u \in L^2(\mathcal{M})$ can be decomposed in the previous basis:

$$u = \sum_{i=0}^{+\infty} u_i \phi_i \text{ , with } u_i = \int_{\mathcal{M}} u\phi_i. \tag{2}$$

The Parseval's formula which will be useful for normalization states that :

$$\int_{\mathcal{M}} u^2 = \sum_{i=0}^{+\infty} u_i^2. \tag{3}$$

It is possible to compute eigenfunctions on a mesh $\mathcal{M}_h$ that approximates $\mathcal{M}$ using a weak formulation of the eigenvalue problem and the finite elements method. If u and λ are solutions of $-\Delta_{\mathcal{M}} u = \lambda u$ then:

$$\int_{\mathcal{M}} g(\nabla u, \nabla v) = \lambda \int_{\mathcal{M}} uv \text{ , } \forall v \in L^2(\mathcal{M}). \tag{4}$$

We use the finite elements framework to derive a matricial expression of this weak formulation. We consider the mesh $\mathcal{M}_h$ composed of N vertices. For each vertex i of the mesh we have a function $w_i : \mathcal{M}_h \to \mathbb{R}$ which is continuous, linear on each triangle of the mesh and satisfying the property $w_i(j) = \delta_{ij}$. Any function continuous and linear on each triangle can be decomposed on this basis $u = \sum_{i=1}^{N} u_i w_i$ where u_i are real coefficients. So the equation (4) can be rewritten in the discrete setting, taking $v = w_j$ for all $j \in [1 : N]$. And the discretized problem becomes to find a vector $[U] = (u_i)_{i=[1:N]}$ and a scalar λ such that:

$$[\nabla][U] = \lambda[M][U], \tag{5}$$

with the stiffness and mass matrices given by :

$$[\nabla] = \left(\int_{\mathcal{M}_h} \nabla w_i \cdot \nabla w_j \right)_{i=[1:N], j=[1:N]}, \; [M] = \left(\int_{\mathcal{M}_h} w_i w_j \right)_{i=[1:N], j=[1:N]}.$$

More details on the computation of these two matrices are given in (Desbrun et al., 1999). The eigenvalue problem (5) can be solved for example with

the Lanczos method as in (Arnoldi Package) since the matrices involved are sparse and symmetric positive.
In practice, we computed several thousand eigenfunctions (5000) such that the spatial wavelength reaches a reasonable spatial resolution (see Appendix B). Recent strategies could be investigated to compute sequentially an increasing list of eigenvalues (Vallet and Lévy, 2008) until obtaining the required resolution.

2.5. Curvature decomposition

We used the mean curvature H of the cortical surface to represent its folding pattern. The mean curvature is the average of the two principal curvatures or equivalently half of the trace of the second fundamental form (Petitjean, 2002). Whether in theory we could have used the intrinsic Gaussian curvature, we preferred to use the mean curvature instead because, being an extrinsic measure (dependent on the embedding of the surface in space), it may add supplementary information to the LBO-based decomposition which is already intrinsic to the surface.

The mean curvature can be decomposed in the eigenfunction basis through formula (2). We will denote $H_n := \int_{\mathcal{M}} H\phi_n$ the coefficients of the curvature in the eigenfunctions basis ϕ_n and call *raw spectrum* the sequence $RS_H(n) := H_n^2$. We define also a normalized spectrum of curvature:

$$NS_H(n) := \frac{H_n^2}{\int_{\mathcal{M}} H^2} \qquad \forall n \geq 0. \tag{6}$$

which satisfies:

$$\sum_{n=0}^{+\infty} NS_H(n) = 1 \tag{7}$$

thanks to Parseval's formula (3).

We call *Total Folding Power* the quantity:

$$TFP_H := \sum_{n=0}^{+\infty} H_n^2 = \int_{\mathcal{M}} H^2 \tag{8}$$

This dimensionless parameter is independent of homothetic brain size variation. Namely, if one has a scaling coefficient λ between $\mathcal{M}_1$ and $\mathcal{M}_2$ then $H_{\mathcal{M}_2} = \frac{1}{\lambda} H_{\mathcal{M}_1}$ and a small quantity of surface becomes $dS_2 = \lambda^2 dS_1$,

and then:

$$\int_{\mathcal{M}_2} H^2_{\mathcal{M}_2} dS_2 = \int_{\mathcal{M}_1} H^2_{\mathcal{M}_1} dS_1 \tag{9}$$

See Fig. 2 for computation steps.

2.6. Spectral frequency bands design

In the following, we will call $F(n)$ and $WL(n)$ the theoretical frequencies and the wavelengths associated to the nth eigenfunction (see Appendix A for further development on spatial frequencies):

$$F(n) = \frac{\sqrt{\lambda_n}}{2\pi} \qquad WL(n) = \frac{2\pi}{\sqrt{\lambda_n}} \tag{10}$$

As a consistency check we compared these theoretical frequencies with eigenfunction-derived quantities of the same dimension, which can be intuitively considered as empirical frequencies and can be computed based on the number of nodal domains through the formula:

$$WL2(n) = \sqrt{\frac{\text{Surface of } \mathcal{M}}{\text{Number of nodal domains of } \phi_n}} \tag{11}$$

The raw spectrum of curvature is a very complex type of data, challenging to analyze and even to visualize because of its several thousand points. Moreover, since the eigenfunction bases are defined on a per-individual basis, there is no mathematically exact matching of eigenfunctions of the same n-order (Knossow et al., 2009; Lombaert et al., 2011). Hence, as a dimensional reduction and smoothing step, we merged levels of successive orders into superior grouping levels defined by a sequence of spatial frequency $F(n)$ marking interval limits. The sequence was chosen in order to fulfill a model of branching with doublings of spatial frequency. The spatial frequency associated with the 1st non-constant eigenfunction was considered as the subjects reference frequency $F(1)$. The following interval limits were the spatial frequencies $2^k F(1)$. This merging strategy allowed us to define a band power spectrum (than could be later normalized or not) defined as:

$$BS_H(0) = H_0^2 \tag{12}$$

$$BS_H(k) = \sum_{n=n_1^k}^{n_2^k} H_n^2 \text{ with} \tag{13}$$

$$n_1^k = \arg\min_n |F(n) - 2^{k-1}F(1)| \quad (14)$$

$$n_2^k = \arg\min_n |F(n) - 2^k F(1)| \quad (15)$$

As we computed around 5000 eigenfuntions, this merging strategy allowed us to define 7 bands, numbered from B0 to B6. See Fig. 3 for band design step.

2.7. Spectral segmentation of CFP

We define a CFP map as the binary map where sulci correspond to regions of negative curvature and gyri correspond to regions of positive curvature. Based on the properties of spectral decomposition, band-by-band spectral synthesis of curvature can be performed in a cumulative or non-cumulative way. Non-cumulative synthesis is equivalent to band-pass filtering, and can be used to show the specific contribution of each spectral band. Cumulative synthesis, is equivalent to low-pass filtering, and can be used to show the effect of the gradual addition of higher frequency components to the map. From these 2 types of synthesis, we derived 2 segmentations of CFP:

- First, a segmentation according to the locally dominant frequency band: we used non-cumulative synthesis to label each vertex with the number of the band that contributed the most to its curvature value. See Fig. 4 for computation steps.

- Second, a segmentation according to the locally patterning frequency band: we used cumulative synthesis to label each vertex with the number of the band that determined whether it belong to the sulcal or the gyral pattern. We assessed the differential contribution of each frequency band to the CFP by subtraction between the CFP maps of two consecutive levels of cumulative synthesis. See Fig. 5 for computation steps.

Extensive formulations for these 2 types of segmentation are given in Appendix C. For the sake of clarity, they can be both visualized with a gyral pattern mask, hence restricting the image to the sulcal pattern. Due to their large preponderance in patterning (see Results), second segmentation is restricted to the last three frequency bands.

For each label, we computed the surface area and the number of parcels, i.e. sets of connected vertices that have the same considered label. The segmentation according to the locally dominant band is rather noisy due to the

use of a truncated spectrum (number of eigenfunctions < number of vertices), which produces very small parcels (mainly isolated vertices) related to non-computed bands (very high frequencies). We used an adaptive-threshold filter to remove these noisy parcels before computation (see Appendix B). Conversely, for the segmentation according to the locally patterning band, the number of parcel related to each label had been directly computed on the intermediary subtraction step.

2.8. Statistical analysis and allometric scaling

We preformed an ANOVA to assess the effect of age, sex, and hemispheric volume on hemispheric surface area and spectral parameters. The correlations between cortical surface parameters (hemispheric surface area, total folding power or spectral band power) and brain size (hemispheric volume) were tested assuming a power law:

$$Y = bX^a \tag{16}$$

We compared the scaling factor a in the equation with the value it should have when the scaling is isometric, i.e., presuming that 1 or 2 dimensional parameters scale with hemispheric volume as the 1/3 or 2/3 power respectively and that folding power is constant. The estimation of a and b was performed using log-log linear fit.
All statistical analyses have been performed using SPSS version16.0.

3. Results

3.1. Measuring properties: size and power

3.1.1. Wavelength for domain sizing

The measuring properties of the proposed band power spectrum rely on the association of each LBO eigenfunction of the basis with a well-defined spatial frequency. Eigenfunctions of increasing order (i.e. smaller associated eigenvalue) show an increasingly scattered nodal domain pattern, consistent with the expected increase of their associated spatial frequency (Fig. 3a). The consistency between the empirical wavelength estimated through the number of nodal domains and the theoretical wavelength derived from the eigenvalue is confirmed by the strong linear correlation between the two values. For low orders, the empirical computation is not precise, due to its sensitivity to domain shape, coalescence and irregularity, but from the 10th

order on, the relationship becomes almost exact (mean fit for ICBM database: $0.87x + 4.51$, R = 1), and after the 100th order, there no longer seems to be any difference ($0.97x+0.56$, R = 1). In spite of a certain variability, the mean shape for the nodal domains of an eigenfunction looks like a spot scaled by its theoretical wave length (Fig. 3b). The wavelength not only depends on the order of the eigenfunction but also on the size of each individual brain. Being a one-dimensional parameter intrinsically derived from the grey/white surface, the theoretical wavelength is expected to scale as $HA^{1/2}$, which is almost exactly what we observe in the ICBM database: $1.74GWI^{0.495}$, R = 0.938. This result validates the possibility of computing frequency band statistics in the ICBM database (Table 1).

3.1.2. Spatial resolution concerns

The spatial resolution of our spectral analysis is limited intrinsically by the mesh resolution, and extrinsically by the number of eigenfunctions computed in the decomposition basis. The density of vertices in the surfaces that we used is not homogenous and changes locally depending on the surface geometry. The mean number of vertices in our surface reconstructions was 21418 ± 2268, and the mean triangle edge length was 2mm $\pm$0.5 mm, i.e., a mean resolution of 3mm^2. The mean wavelength of the last eigenfunction necessary to compute the proposed 7 bands is 7mm, i.e. a mean resolution of 9 mm^2 (see Table 1 for values, Fig. 3b for illustration, and Appendix B for computation). Hence, in our analyses the spatial resolution of the decomposition basis was slightly larger than that of the surface meshes. This allowed us to consider a minimal pattern element of around 3 contiguous vertices. This resolution is reasonable given that the patterns of interest in a cortical surface are hardly to be found below half a centimeter, and also to avoid variation due to inaccuracies in surface segmentation and reconstruction. To assess the robustness of our results with respect to the number of vertices of the meshes, we compared the spectrum computation before and after mesh refining (doubling of the number of vertices) , and we did not find any significant differences (data not shown).

3.1.3. Band power proportions

By construction, the proposed band power spectrum gives a partition of the total folding power in intervals of doubling spatial frequencies (i.e. spectral bands). The band power spectrum normalized by the total folding power provide a spectral proportion, or in other terms, the relative weight

of each spectral band. However, the decomposition basis necessary for the computation of 7 bands cannot account for the full total folding power since part of it is contained in the higher frequency levels that we do not compute. The normalized 7 bands spectra of all ICBM database subjects shows that on average, our analysis concerns around 2/3 of the total folding power (mean 65.8%, SD 1.45%, Fig. 6). More precisely:

- B0 (the constant band) accounted for 0.35% (SD 0.14%),
- B1, 2 and 3 (the first 3 oscillating bands) accounted for 4.39% (SD 0.79%),
- B4, 5 and 6 (the last 3 oscillating bands) accounted for 61.2% (SD 1.43%).

This shows the quantitative predominancy of the last 3 bands, which account for a large proportion of the total folding power and almost the totality of the analyzed folding power (92.8%).

3.2. Describing properties : anatomo-spectral correlations

We now show the utilization of Spangy to categorize and quantify pattern elements back on the original cortical surface, on the basis of spatial frequency properties.

3.2.1. Global shape vs folds patterning

Low-pass and band-pass filtering provide a first insight into the link between spectrum and cortical folding through the sequential visualization of the contribution of each band to the curvature value (Fig. 4) and the CFP (Fig. 5). B0 does not account for any pattern since the 1st eigenfunction does not oscillate. B1 and B2 bands account for patterns that are not correlated with folding but rather with the global brain shape, like the slight concavity of the medial hemispheric side (B1) and the bottom of the sylvian fissure (B2), the global convexity of the lateral hemispheric side (B1), or the convexity of the polar regions (B2). B3 contributes mainly to the global brain shape with the transition between lateral and medial sides of the hemisphere or the sylvian banks, but also to initiate the fundi of several primary sulci, such as the posterior part of the superior temporal sulcus or the medial part of the intra parietal sulcus. As we shown previously, whatever the qualitative contribution to the CFP of the first three non-constant bands may be, they

are quantitatively very weak. Thus, patterns consistent with cortical folding appear with B4 (Fig. 4, Fig. 5) and most substantial contributions to the CFP are produced by B4, B5 and B6. These 3 bands will be further referred as the folding bands.

3.2.2. Dominant vs patterning band for segmentation of CFP

The 2 types of spectral segmentation of CFP (Fig. 4 and Fig. 5) are presented in Fig. 7 on 5 brains of increasing size (restricted to sulcal pattern): the segmentation according to patterning band in the 2nd column, and the segmentation according to dominant band in the 3rd column. They provide complementary information about the contribution of each folding band. The segmentation according to patterning band sums up the observations made on low-pass filter series and provides a clear image of the progressive ramification of the sulcal pattern produced by the addition of higher frequency bands. The segmentation according to dominant band shows a similar phenomenon but with significant differences in surface labeling which show that a vertex can be added to sulcal or gyral pattern by one band, whereas its curvature value is mainly determined by a higher frequency band. These discrepancies between a locally patterning frequency band and locally dominant frequency band are particularly visible around the polar regions. Besides, as previously explained, the segmentation according to dominant band is noisy and we applied a band-adapted minimum threshold for size before the quantification of surface area and number of sulcal parcels. This threshold had a very mild effect on the regions labeled by B4, B5 and B6, leading to a mean area reduction of respectively 6.9%, 1% and $< 0.1\%$(SD 1.5%, 0.2% $< 0.1\%$). Nonetheless, it was sufficient to rub out most of the irrelevantly small spots, particularly for B4 band, rejecting an average of respectively 118, 45 and 3 spots (SD 19, 11 and 2), with a mean spot area 2 times below the threshold. Finally, we found a strong linear correlation between B4, B5 and B6 spectral power and labeled surface area, respectively: $335x + 3660$ ($R = 0.783$), $396x - 96.3$ ($R = 0.917$), $403x + 884$ ($R = 0.961$), showing that the segmentation according to dominant band gives a faithful picture of the band power spectrum. The correlation was equally good between the normalized band power and the labeled surface area reported to hemispheric surface area.

3.2.3. Anatomical correlates of spectral segmentation of CFP

The sulcal pattern of the low-pass filtered CFP map at B4 level consists in a limited set (21 elements ± 3) of large smooth sulcal parcels with few ramifications (Fig. 7, 1st column). These spectrally defined folding fields embed the main primary folds of the literature (Fig. 8a, (Chi et al., 1977)) and are refined by B5 and B6 to produce a more irregular and branched CFP. Thanks to the proposed spectral segmentations, the CFP can be divided into 1st, 2nd and 3rd order elements associated respectively with frequency bands B4, B5 and B6. A segmentation considering only the folding bands is supported by the restriction of lower frequency band labeling exclusively to B3 for a few deep sections of the superior temporal sulcus, intra parietal sulcus or insula, covering a very small percentage of the total sulcal area ($< 5\%$). The anatomical correlates of this division are well illustrated by the analysis of the pericentral region in 3 reference brains of increasing size (Fig. 8). The figure shows the straight course of the 1st order central element, the 2 or 3 loops corresponding to 2nd order elements and the small dimples associated with 3rd order elements, which are much more accentuated in the larger brain. The increasing order for pattern elements in ramifications is also visible in the post central sulci. The impression of extension of B4 or even B5 labeling into higher ramification is drawn by the fact that gyral pattern elements are masked on most of the presented segmentations (due to legibility concerns for figures). Indeed, the same anatomical correlation can be observed for gyral pattern and yet, for the whole CFP (Fig. 8c). Hence, we show that the distribution of 2nd and 3rd order elements of pattern is neither random nor homogeneously underlying the limits of lower order elements, but rather parsimoniously matches the gradual ramification of CFP from the previously defined 1st order folding fields.

3.3. Spectral composition of CFP as a function of brain size

3.3.1. Surface area and folding power scaling

We used the hemispheric volume (HV) as a brain size parameter. In our dataset, HV ranged from 445 cm3 to 759 cm3, i.e., a 1.7-fold variation (Table 1). The hemispheric surface area showed a positive allometric scaling: $HA = 0.209HV^{0.961}$ (R = 0.950, $p < 0.001$, confidence interval $[0.935, 0.987]$), i.e. large brains had disproportionately more cortical surface than smaller brains. We found the same variation with brain size for the sulcal pattern area and the gyral pattern area, showing the absence of allometric modification of sulcal versus gyral proportions: sulcal pattern

area=$0.127HV^{0.951}$ (R = 0.953, $p < 0.001$, confidence interval $[0.926, 0.976]$) ; gyral pattern area=$0.0828HV^{0.972}$ (R = 0.898, $p < 0.001$, confidence interval $[0.934, 1.012]$). Total folding power also showed a positive allometric scaling, consistent with the fact that large brains are not simply scaled-up versions of smaller ones: total folding power=$8.16 \times 10^{-3} HV^{0.781}$ (R = 0.784, $p < 0.001$, confidence interval $[0.73, 0.832]$). We used these allometric exponents as references for the scaling exponents we found for subdivisions of the hemispheric surface (1st, 2nd and 3rd order elements of CFP) and total folding power (B4, B5 and B6).

3.3.2. Spectral allometry: different brain size means different spectral proportions

As they accounted for more than 90% of the analyzed folding power, we limited the following analysis to the folding bands. The largest proportion of the variance in spectral band power was related to brain size variation (R^2=61% in a centered model) with no significant effect of age, sex, or handedness. Normalized band spectrum revealed a significant effect of brain size on spectral proportions (Fig. 6c). Large brains (standard score for $HV > Mean+1SD$) showed a significantly larger proportion of B6 high spatial frequencies than small brains (standard score for $HV < Mean - 1SD$) and conversely, they showed a smaller proportion of B4 low spatial frequencies ($p < 0.001$ in both cases). The proportion of B5 medium spatial frequencies was not significantly different between the large and small brains. To further investigate the relationship between brain size and curvature band power spectrum we compared the scaling of each spectral band power with the scaling of total folding power. We found no correlation between brain size and folding power for B4, an allometric exponent similar to that of total folding power for B5 (0.753 ± 0.052 versus 0.781 ± 0.051) and a higher allometric exponent of for B6 (1.213 ± 0.061 versus 0.781 ± 0.051). This shows that in large brains the larger proportion of B6 spatial frequencies compared with B4 and B5 is due to an increased contribution of these high frequencies to CFP rather than a decrease of B4 ones (Fig. 9 b). It also explains the stable proportion of B5 frequencies since total folding power is the normalization constant. In other terms, B4 contribution to the CFP is independent of brain size i.e. isometric scaling, B5 contribution follows the average increase of folding power with brain size i.e. positive allometric scaling, and B6 contribution increase faster than average i.e. the positive allometry is stronger for the higher spatial frequencies.

3.3.3. Complexification of CFP with brain size

How do the different behaviors of each folding band translate in terms of CFP? The computation of surface area and number of sulcal parcels for each label of the segmentation according to dominant band is presented in Fig. 9c, d. The variation of surface area with brain size for each order of CFP elements showed a specific behavior similar to that of frequency band power: increase of area with brain size is very slow for 1st order (B4 label), parallel to surface extension for 2nd order (B5 label) and faster than expected for 3rd order (B6 label). This result was robust and not sensitive to filter suppression. The number of parcels was independent of brain size for 1st and 2nd order i.e. constant in spite or surface extension, whether the number of parcels increased for 3rd order (Fig. 9d). This result was sensitive to filter suppression but we found the same behavior for each order with the segmentation according to patterning band that provides an even clearer image of the progressive ramification and do not require filtering (Fig. 9e). We found no significant differences between the analysis confined to the sulcal pattern and that of the whole CFP. Hence, in terms of CFP, the proposed spectral segmentation allows a characterization and quantification for complexification with brain size demonstrating that it consists in a high frequency ramification already suspected by visual comparison of smaller and larger brain of the dataset (Fig. 7 and Fig. 8).

4. Discussion

The proposed Spectral Analysis of Gyrification (Spangy) methodology achieves a categorical and quantitative analysis of cortical folding pattern (CFP) both in the frequency domain through a band power spectrum and in the image domain with an anatomically relevant spectral segmentation. The computation is directly carried on native data without the need for spherical parametrization or template normalization. The choice of the mean curvature of the grey-white interface for CFP depiction could be questioned. Theoretically, any other continuous scalar function defined on a cortex derived surface mesh could have been elected. Does any other would give a more accurate rendering for folds? Actually, the mean curvature defines two gyral and sulcal patterns of almost equal area on the grey-white interface, but not on external cortical surface (i.e. pial surface) where the CFP is very unbalanced. Future application of Spangy should probably try to analyze this external surface or even an intermediate surfaces such as proposed by

Van Essen (**?**) [Ref ?], It would also be of interest to look for invariants between spectra computed on the same brains but with different choices of surface or folding proxy (gaussian curvature, sulcal depth, etc.). Besides, the choice of the surface and its computation could affect the spatial resolution of the analysis. Indeed, if secondary mesh refinement (computational vertex density augmentation) does not seems to impact much on results, a primary higher mesh resolution could bring new spatial frequencies components out of the background noise, requiring an expansion of the eigenfunction basis to avoid aliasing.

The properties of Spangy rely on our frequency bands design and frequency modeling choices. The a priori definition of band limits starting from the first non-null frequency appeared to us as the simplest strategy. First, merging the raw spectrum into bands of doubling spatial frequency provides an objective method to compare different subjects. However, inter subject matching between eigenfunctions of the same order is a difficult problem, which complicates full ordinal comparison between extended raw spectra (Knossow et al., 2009; Lombaert et al., 2011). This discrepancy exists both for nodal domain pattern and exact associated wavelength. Nonetheless, the proposed large frequency bands realize a large scale smoothing in the frequency space resulting in a strict inter subject frequency matching between bands of the same order. It is worth noting that this matching is up to a proportional factor given by the wavelength associated with the first non-null eigenvalue ($WL(1) = 1/F(1)$). This factor, which is proportional to $HA^{1/2}$, can be seen as the geodesic length of the hemisphere (Lefèvre et al., 2012) and could be used as a surface based normalization factor of eigenfunction basis associated wavelength. In other terms, Spangy depicts CFP with a scale of brushes adapted to object size: larger touches are required for larger brains. Furthermore, analytic effects of the merging strategy strongly depend on the frequency model chosen for band splitting. We could have elected an arbitrary sequence of bands, such as quadratic sequences (limits associated with $k^2F(1)$), but we found few obvious anatomical correlations for the resulting spectra (data not shown). The proposed $2^kF(1)$ sequence presents at least 3 very convenient properties :

- it allows a good degree of compaction.
- it segregates the folding bands that clearly contribute to CFP from those that seem to account for global shape.

- it leads to a segmentation of pattern ramifications.

The first property was obviously expected from high growth rate of $2^k F(1)$ sequence.
The second one could not be anticipated and we still have no model for sulcal pattern apparition with B4, that is to say $2^3 F(1)$ to $2^4 F(1)$ spatial frequency range. Since this range is quantitatively large and the density of eigenfunction still rather low in this zone of the spectrum, the matching is probably not exact and there is probably no exact frequency threshold above which CFP arises. This uncertain area concerning exact delineation of spectral folding frequency domain pleads for future implementation of intelligent models such as machine learning algorithm for CFP fundamental frequency assessment or for frequency clustering, with or without anatomically labeled learning data base (i.e., in a supervised or unsupervised way). Nonetheless, the present strategy designs a convincing first folding band from which models of frequency doubling makes sense. Our primary interest in CFP analysis should not overshadow the clear emphasis of low frequency bands association with curvature variations related to global shape. Though quantitatively small compared with the folding bands, recent works suggest that the information gathered into these low frequencies may be neuroscientificaly relevant, at least for global shape classification (Niethammer et al., 2007; Lai et al., 2009).
As for the third property, it results from the main hypothesis of the frequency model, namely, the doubling of frequency with pattern extension. Our results in terms of spectral segmentation of CFP clearly show that this hypothesis is consistent with true anatomical data. Interestingly, the bandwidth of the folding bands may partially accommodate the variation of dominant wavelength of same order elements of pattern between different regions of the brain, such as polar regions where the patterns seem to be tighter and central where they seem wider. At least it seems true with the segmentation according to the locally patterning frequency band. With Spangy native data strategy, this classical phenomenon on a surface with spherical topology is accurately revealed and not artificially accentuated by spherical parametrization.

The accuracy and consistency of the spectral segmentation of CFP that we obtained is indeed an important concern. Apart from the frequency doubling hypothesis, the segmentation proposed is free from anatomical or de-

velopmental a priori. Labeling is then based only on spatial frequency characteristics of local curvature variations, or more precisely on how this local variation integrates into the whole pattern since spectral analysis is not a local analysis. The results of our analysis of the central region show that we can distinguish two types of gradual contribution of the folding bands: firstly the termination of elongated elements of pattern, secondly the ramification of pattern both from an existing element and de novo. Termination labeling is of little anatomical meaning and rather due to later discussed strong impact of depth on surface based wavelength. Conversely, ramification labeling is an interesting achievement. Indeed, starting from spectrally defined primary folding fields, Spangy segmentation categorizes 2nd and 3rd order of ramification or complexification of CFP in a way that only developmental longitudinal follow-up had authorized up to know (Chi et al., 1977). To our knowledge, no other strictly morphological analysis achieved this type of result. Recent closely related mathematical tools such as fractal modeling (Yotter et al., 2011) allows to estimate at global, regional and local scales, a fractal dimension of the cortical surface thanks to spherical harmonics but the authors have not applied their methodology to the characterization of normal CFP. More intuitively, Laplacian smoothing has been presented several times as a possible tool for categorization of elements of sulcal pattern since supposedly tertiary fold seems to disappear earlier in the process than secondary, and so on (Cachia et al., 2003). Unfortunately, it is a continuous process depending on a scale parameter t whose relevant values vary from a fold to another and across subjects. It is interesting also to note that this process is not mathematically equivalent to filtering even if smoothing a map u till time t can be expressed from eigenvectors and eigenfunctions of Laplace-Beltrami Operator:

$$S(u)(t) = \sum_{i=0}^{+\infty} u_i e^{-\lambda_i t} \phi_i \tag{17}$$

which is different from a truncated expression of equation (2):

$$F(u)(N) = \sum_{i=0}^{N} u_i \phi_i \tag{18}$$

Besides, many regions are much more intricate than the central region where categorization of CFP elements is probably unattainable locally, at

least in the image space. This is another advantage of the proposed spectral analysis, which integrates the whole pattern information in the frequency space for band power spectrum computation, but returns part of it locally in the image space with the segmentation according to the locally dominant frequency band. Hence, we are able to propose a spectral based segmentation even in a more difficult region such as prefrontal cortex. On that matter, regional implementation of our spectral strategy on a patch of mesh corresponding to a lobe or a functional area (Broca for instance) is of possible interest. Nonetheless, further demonstration of concordance between spectral and developmental labeling for elements of CFP still exceeds the aim of the present work and certainly need more investigation, for instance on longitudinal data. Indeed, it is of important concern to try and validate on real biological data the different folding models proposed in the literature (Thompson et al., 1996; Mora and Boudaoud, 2006; Striegel and Hurdal, 2009; Yotter et al., 2011). To a certain extent, the anatomical consistency of Spangy spectral segmentation brings a new point to the models that predict a frequency doubling with folding extension.

Besides its categorial properties, Spangy provides two types of quantitative information.
Firstly, the wavelength intervals associated with B4, B5 and B6 give a size for 1st, 2nd and 3rd order elements of CFP that can be seen as a surface-based or geodesic wavelength. Such a surface-based measure depends both on the local depth and the local width of the associated fold. Very few object-based morphometric data are available for cortical folds. The BrainVISA morphometric toolbox allows maximum and mean depth assessment for well validated sulci models but provides no ramification-based segmentation. Nevertheless, the magnitude order for central sulcus is consistent with B4 associated wavelength range (Mangin et al., 2004). Object-based definition and computation of other size parameters such as volume-based (Euclidian) or surface-based (Riemanian) wavelength would be of great interest to compare with the measures provided by Spangy. Indeed, accurate CFP morphometry could open the field to a new quantitative characterization of folding during development or in congenital malformation such as lissencephaly (too few, too large folds) of polymicrogyri (too many, too tight folds) (Richman et al., 1975). But these two examples also emphasize that sizing of CFP elements is no enough for such a characterization, one needs to be able to give the global composition of CFP for each category.

This is precisely the second quantitative information provided by Spangy. Each folding band power is probably the best assessment of each spatial frequency interval to the CFP since spectral segmentation goes with certain loss of information: locally, an element of pattern can only be related to one band even if several folding orders are intricate. Nonetheless, back in the image, useful ramification count is allowed by CFP spectral segmentation. Here again, a regional analysis could be proposed by looking for lobar or functional area dominant frequency variations.

In this work we propose a first application of this new insight provided by Spangy to the question of the relationship between brain size polymorphism and CFP complexity variation. The allometric relationship between brain size (hemispheric volume) and hemispheric surface area has been already reported (Toro et al., 2008). Some results even suggest that this allometry is not spatially homogenous and that local gyrification indexes seems to increase more in some brain regions than in others, prefrontal area for instance (Toro et al., 2008; Schaer et al., 2008). Gyrification indexes inform us on the amount of buried cortical surface but give no information about CFP. About this concern, hemispheric total folding power behaves as hemispheric gyrification index: they are highly correlated but both equally blind to shape and gyrification pattern ($R = 0.8$). The band power spectrum provided by Spangy precisely unwraps this black-box to reveal 3 orders of pattern elements of 3 increasing spatial frequency bandwidth which behave differentially with brain size and total folding pattern increase. Complexification of gyrification can be seen as an extension of CFP both by ramification and addition of disconnected new elements of pattern. Our results show that this type of complexification occurs with increasing brain size since the contribution to CFP of B4 low spatial frequencies is constant in terms of spectral power and number of pattern elements, the one of B5 medium spatial frequencies increase with the same allometric exponent than total folding power but with a number of pattern elements still constant, and the one of B6 high spatial frequencies shows both a much higher allometric exponent and an augmentation of number of pattern elements. To our knowledge, this is the first objective and quantitative demonstration of this allometric phenomenon suspected from radiological observations. Large brains are definitely twister because of an increased number of barbells, dimples and kinks of high spatial frequency that accommodate the allometric increase of cortical surface to be buried.

5. Conclusion

At the end.

Appendix A. Definition of spatial frequencies

In one dimension, the eigenvalue problem (1) becomes

$$u''(x) = -\lambda u(x) \qquad \forall x \in [0, L] \tag{A.1}$$

and the solutions are obtained through the sine and cosine functions depending on boundary conditions (Dirichlet or Neumann for instance). An eigenfunction can be expressed on the form $\cos(\frac{\pi n x}{L})$ or $\sin(\frac{\pi n x}{L})$ with n an integer that gives the number of oscillations of the eigenfunction and the corresponding eigenvalue is $\lambda_n = (\frac{\pi n}{L})^2$. The frequency is classically defined as the inverse of the period or wavelength $\frac{2\pi}{\pi n/L}$ and therefore equals $\frac{\sqrt{\lambda_n}}{2\pi}$. In two dimensions we can have explicit formula in the case of a rectangular domain of size L and l and the eigenfunctions can be expressed in a decoupled way, for instance for Neumann boundary conditions:

$$\cos\left(\frac{\pi m x}{L}\right)\cos\left(\frac{\pi n y}{l}\right) \qquad \forall (x, y) \in [0, L] \times [0, l] \tag{A.2}$$

and the corresponding eigenvalue is $\lambda_n = (\frac{\pi m}{L})^2 + (\frac{\pi n}{l})^2$. Even if the concept of spatial frequency is ambiguous in 2D and depends on the oscillations along each direction x and y, we will consider that $\sqrt{\lambda_n}$ has the dimension of a spatial frequency.

Appendix B. Computation of resolution and thresholds

For a given spatial resolution of a mesh, let d be the average edge distance between two contiguous vertices. Then, the average sign inversion spot (an isolated point of different sign than its neighbors) is around $\pi(d/2)^2$ mm^2 large (small disc of d mm diameter). For a given eigenfunction basis spatial resolution, let WL be the wavelength associated with last eigenfunction of the basis. Then, it is associated with an average size spot of $\pi(WL/4)^2$ area (small disc of $WL/2$ mm diameter).

For the adaptative thresholding in 2.7, we have made a similar reasoning: a noisy parcel in band k is roughly approximated by a circular shape of radius R_k. So we have the relation for the characteristic size :

$$2R_k < \frac{1}{2}\frac{WL(1)}{2^k} \tag{B.1}$$

which implies that the area of the parcels satisfiies:

$$A_k < \frac{\pi^2}{16}\left(\frac{WL(1)}{2^k}\right)^2 \tag{B.2}$$

The adaptative threshold for each spectral band k is therefore given by the right term in the previous equation.

Appendix C. Extensive formulations of the spectral segmentations

We give here the formula for the segmentation according to the locally dominant frequency band:

$$MBC(p) = \arg\max_{k>0}\left(\text{sign}(H(p))\sum_{n=n_1^k}^{n_2^k} H_n\phi_n(p)\right) \quad \forall p \in \mathcal{M} \tag{C.1}$$

The sign of the curvature indicates whether we are in a gyrus or a sulcus.

For the segmentation according to the locally patterning frequency band, we start by computing the differential contribution of each frequency band to the CFP by subtraction between the CFP maps of two consecutive levels of cumulative synthesis :

$$\forall p \in \mathcal{M} \quad SM_k(p) = a - b \text{ where} \tag{C.2}$$

$$a = 1 \text{ if } \sum_{n=1}^{n_2^k} H_n\phi_n(p) > 0 \text{ else } a = 0 \tag{C.3}$$

$$b = 1 \text{ if } \sum_{n=1}^{n_2^{k-1}} H_n\phi_n(p) > 0 \text{ else } b = 0 \tag{C.4}$$

Then, we follow the procedure explained graphically in Fig. 5: We start from SM_k for $k = 6$ (third row, first column) which counts 3 labels -1 (blue), 0 (gray) or 1 (red). A vertex with label l will be assigned another label $3l$. Then we consider SM_k for $k = 5$ (third row, second column) and to each vertex with label l not previously re-labeled we assign the label $2l$. The last

step is achieved for $k = 4$ where all vertices not re-labeled previously will keep their label l. Finally, the resulting segmentation is represented with a gyral mask (last row) and counts 3 labels: -3 (green), -2 (cyan) and -1 (dark blue).

Armstrong, E., Schleicher, A., Omran, H., Curtis, M., Zilles, K., 1995. The ontogeny of human gyrification. Cerebral Cortex 5, 56.

Arnoldi Package, . Http://www.caam.rice.edu/software/ARPACK/.

Berger, M., 2003. A panoramic view of Riemannian geometry. Springer Verlag.

BrainVisa Software, . Http://www.brainvisa.info/.

Cachia, A., Mangin, J., Riviere, D., Kherif, F., Boddaert, N., Andrade, A., Papadopoulos-Orfanos, D., Poline, J., Bloch, I., Zilbovicius, M., et al., 2003. A primal sketch of the cortex mean curvature: a morphogenesis based approach to study the variability of the folding patterns. IEEE transactions on medical imaging 22, 754–765.

Cachia, A., Paillère-Martinot, M., Galinowski, A., Januel, D., de Beaurepaire, R., Bellivier, F., Artiges, E., Andoh, J., Bartrés-Faz, D., Duchesnay, E., 2008. Cortical folding abnormalities in schizophrenia patients with resistant auditory hallucinations. Neuroimage 39, 927–935.

Chi, J., Dooling, E., Gilles, F., 1977. Gyral development of the human brain. Annals of Neurology 1, 86–93.

Chung, M., Hartley, R., Dalton, K., Davidson, R., 2008. Encoding cortical surface by spherical harmonics. Satistica Sinica 18, 1269–1291.

Crampin, E., Gaffney, E., Maini, P., 1999. Reaction and diffusion on growing domains: Scenarios for robust pattern formation. Bulletin of Mathematical Biology 61, 1093–1120.

Dale, A., Fischl, B., Sereno, M., 1999. Cortical surface-based analysis* 1:: I. segmentation and surface reconstruction. Neuroimage 9, 179–194.

Desbrun, M., Meyer, M., P., S., Barr, A., 1999. Implicit fairing of irregular meshes using diffusion and curvature flow, in: Proceedings of the 26th

annual conference on Computer graphics and interactive techniques, pp. 317–324.

Fischl, B., Rajendran, N., Busa, E., Augustinack, J., Hinds, O., Yeo, B., Mohlberg, H., Amunts, K., Zilles, K., 2007. Cortical folding patterns and predicting cytoarchitecture. Cerebral Cortex 18, 1973–80.

Gu, X., Wang, Y., Chan, T., Thompson, P., Yau, S., 2004. Genus zero surface conformal mapping and its application to brain surface mapping. Medical Imaging, IEEE Transactions on 23, 949–958.

Hübsch, T., Tittgemeyer, M., 2008. Multi-scale analysis of brain surface data. Mathematical Modeling of Biological Systems, Volume II , 255–263.

Im, K., Lee, J., Lyttelton, O., Kim, S., Evans, A., Kim, S., 2008. Brain size and cortical structure in the adult human brain. Cerebral Cortex 18, 2181.

Knossow, D., Sharma, A., Mateus, D., Horaud, R., 2009. Inexact matching of large and sparse graphs using laplacian eigenvectors. Graph-Based Representations in Pattern Recognition , 144–153.

Kruggel, F., 2008. Robust parametrization of brain surface meshes. Medical Image Analysis 12, 291–299.

Lai, R., Shi, Y., Dinov, I., Chan, T., Toga, A., 2009. Laplace-beltrami nodal counts: A new signature for 3d shape analysis, in: IEEE International Symposium on Biomedical Imaging: From Nano to Macro, ISBI'09, pp. 694–697.

Lefèvre, J., Germanaud, D., Fischer, C., Toro, R., Rivière, D., Coulon, O., 2012. Fast surface-based measurements using first eigenfunction of the laplace-beltrami operator: interest for sulcal description, in: IEEE International Symposium on Biomedical Imaging: From Nano to Macro, ISBI'12, submitted.

Lévy, B., 2006. Laplace-beltrami eigenfunctions towards an algorithm that understands geometry, in: Shape Modeling and Applications, 2006. SMI 2006. IEEE International Conference on, IEEE. pp. 13–13.

Lombaert, H., Grady, L., Polimeni, J., Cheriet, F., 2011. Fast brain matching with spectral correspondence, in: Information Processing in Medical Imaging, Springer. pp. 660–673.

771 Luders, E., Narr, K., Thompson, P., Rex, D., Jancke, L., Steinmetz, H., Toga,
772 A., 2004. Gender differences in cortical complexity. Nature Neuroscience
773 7, 799–800.

774 Mangin, J., Riviere, D., Cachia, A., Duchesnay, E., Cointepas, Y.,
775 Papadopoulos-Orfanos, D., Collins, D., Evans, A., Régis, J., 2004. Object-
776 based morphometry of the cerebral cortex. Medical Imaging, IEEE Trans-
777 actions on 23, 968–982.

778 Mazziotta, J., Toga, A., Evans, A., Fox, P., Lancaster, J., 1995. A probabilis-
779 tic atlas of the human brain: Theory and rationale for its development::
780 The international consortium for brain mapping (icbm). Neuroimage 2,
781 89–101.

782 Mora, T., Boudaoud, A., 2006. Buckling of swelling gels. The European
783 Physical Journal E: Soft Matter and Biological Physics 20, 119–124.

784 Niethammer, M., Reuter, M., Wolter, F., S., B., Peinecke, N., Koo, M., Shen-
785 ton, M., 2007. Global medical shape analysis using the laplace-beltrami
786 spectrum, in: Proceedings of MICCAI, pp. 850–857.

787 Petitjean, S., 2002. A survey of methods for recovering quadrics in triangle
788 meshes. ACM Computing Surveys 34, 211–262.

789 Prothero, J., Sundsten, J., 1984. Folding of the cerebral cortex in mammals.
790 Brain, Behavior and Evolution 24, 152–167.

791 Régis, J., Mangin, J., Ochiai, T., Frouin, V., Riviére, D., Cachia, A., Tamura,
792 M., Samson, Y., 2005. "Sulcal Root" Generic Model: a Hypothesis to Over-
793 come the Variability of the Human Cortex Folding Patterns. Neurologia
794 medico-chirurgica 45, 1–17.

795 Reuter, M., Wolter, F., Peinecke, N., 2006. Laplace-beltrami spectra as []
796 shape-dna'of surfaces and solids. Computer-Aided Design 38, 342–366.

797 Richman, D., Stewart, R., Hutchinson, J., Caviness Jr, V., 1975. Mechanical
798 Model of Brain Convolutional Development. Science 189, 18–21.

799 Schaer, M., Cuadra, M., Tamarit, L., Lazeyras, F., Eliez, S., Thiran, J., 2008.
800 A surface-based approach to quantify local cortical gyrification. Medical
801 Imaging, IEEE Transactions on 27, 161–170.

Striegel, D., Hurdal, M., 2009. Chemically Based Mathematical Model for Development of Cerebral Cortical Folding Patterns. PLoS Comput Biol 5.

Thompson, P., Schwartz, C., Lin, R., Khan, A., Toga, A., 1996. Three-dimensional statistical analysis of sulcal variability in the human brain. The Journal of neuroscience 16, 4261.

Toro, R., Perron, M., Pike, B., Richer, L., Veillette, S., Pausova, Z., Paus, T., 2008. Brain size and folding of the human cerebral cortex. Cerebral cortex 18, 2352.

Vallet, B., Lévy, B., 2008. Spectral geometry processing with manifold harmonics. Computer Graphics Forum 27, 251–260.

Watkins, K., Paus, T., Lerch, J., Zijdenbos, A., Collins, D., Neelin, P., Taylor, J., Worsley, K., Evans, A., 2001. Structural asymmetries in the human brain: a voxel-based statistical analysis of 142 mri scans. Cerebral Cortex 11, 868.

White, L., Andrews, T., Hulette, C., Richards, A., Groelle, M., Paydarfar, J., Purves, D., 1997. Structure of the human sensorimotor system. i: Morphology and cytoarchitecture of the central sulcus. Cerebral Cortex 7, 18.

Whitwell, J., Crum, W., Watt, H., Fox, N., 2001. Normalization of cerebral volumes by use of intracranial volume: implications for longitudinal quantitative mr imaging. American journal of neuroradiology 22, 1483.

Yotter, R., Nenadic, I., Ziegler, G., Thompson, P., Gaser, C., 2011. Local cortical surface complexity maps from spherical harmonic reconstructions. NeuroImage .

Yousry, T., Schmid, U., Alkadhi, H., Schmidt, D., Peraud, A., Buettner, A., Winkler, P., 1997. Localization of the motor hand area to a knob on the precentral gyrus. a new landmark. Brain 120, 141–157.

Zilles, K., Armstrong, E., Schleicher, A., Kretschmann, H., 1988. The human pattern of gyrification in the cerebral cortex. Anatomy and Embryology 179, 173–179.

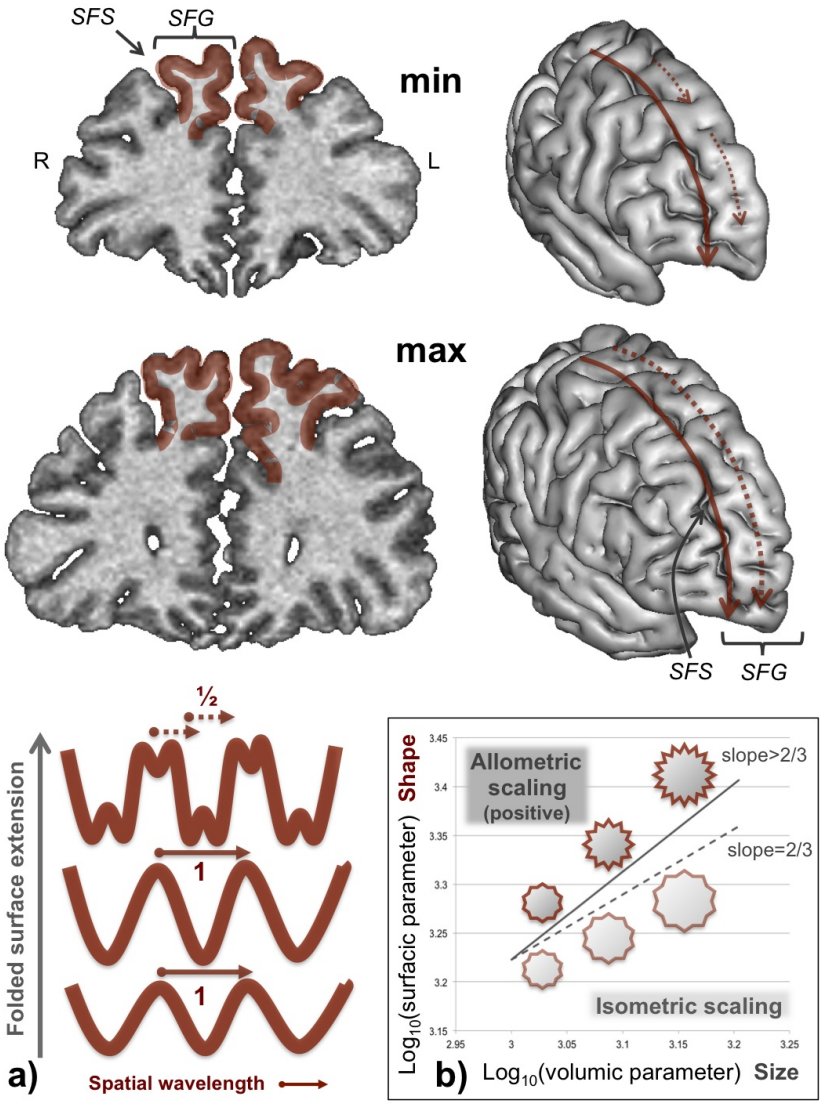

Fig 1: Modeling framework for cortical folding.

a) The doubling frequency hypothesis. 1st row: brain of minimum size of the database 2nd row: brain of maximum size of the database, more folded cortical surface in the SFG 3rd row: theoretical model extrapolated from (Mora and Boudaoud, 2006). Left column: coronal section perpendicular to the ACPC line and tangential to the genu of the corpus callosum (T1-weighted images) Right column: pial surface of the right hemisphere SFS: superior frontal sulcus, SFG: superior frontal gyrus, R: right, L: left.
b) Allometric scaling for cortical folding.

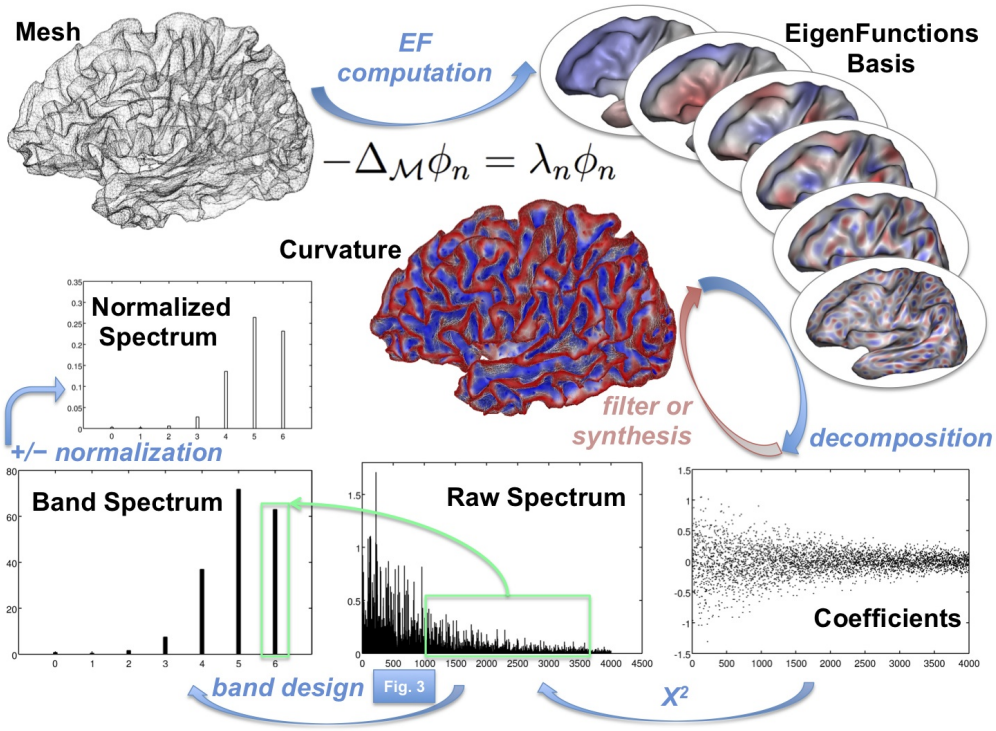

Fig 2: Spangy process

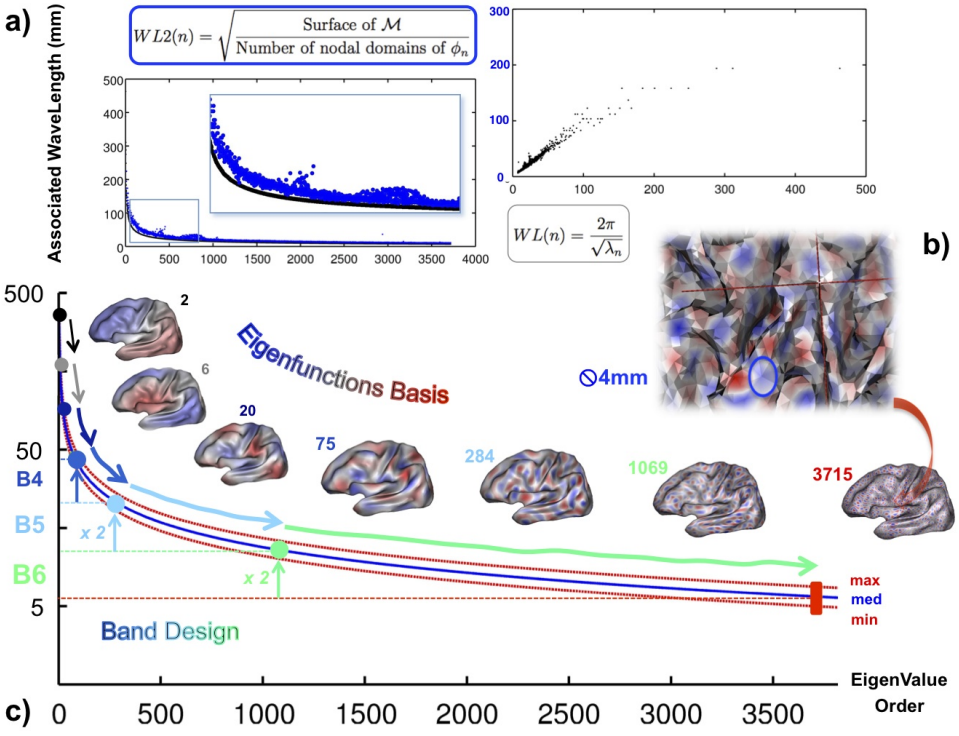

Fig 3: Spectral band design.

a) Eigenfunction associated wavelength (WL). Comparison between theoretical wavelength (black) and empirical one (blue).
b) Spatial resolution. Visualization of the nodal domains of the last eigenfunction of the basis for the median size brain of the database.
c) Spectral bands: limits of the frequency intervals according to the doubling frequency hypothesis. Log-linear plot. min, med, max: brain of minimum, median and maximum size of the database.

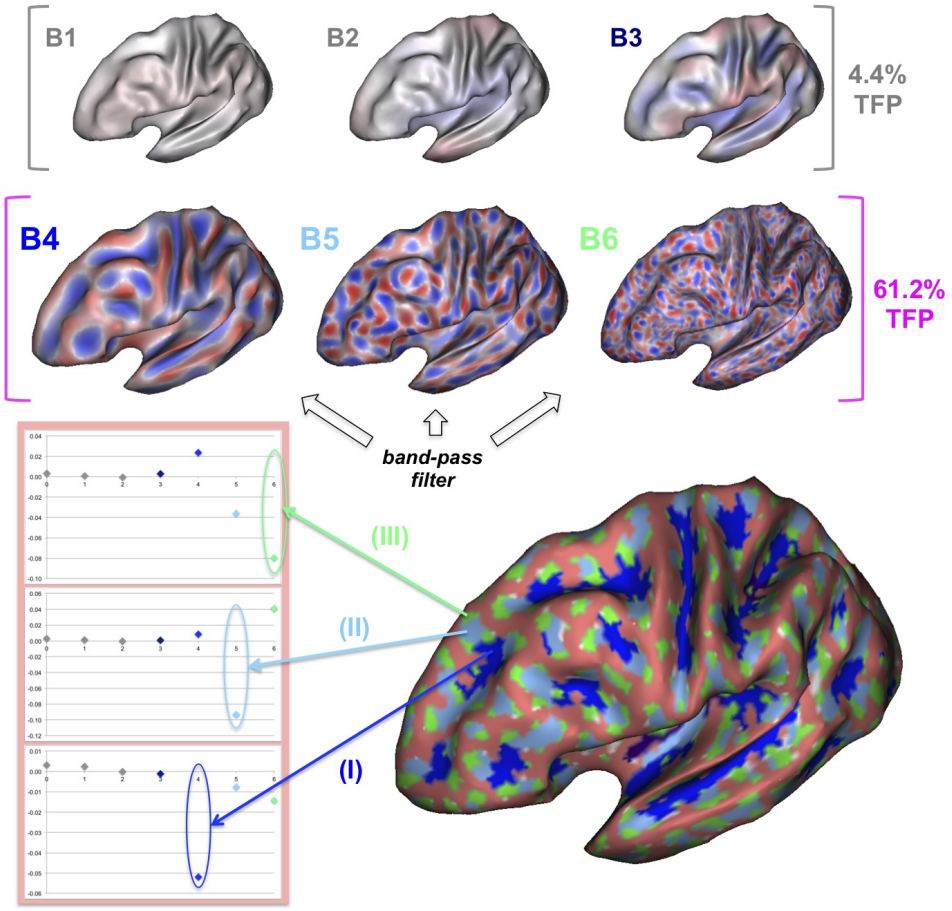

Fig 4: Segmentation of CFP according to the locally dominant band.

1st and 2nd row show the series of band-pass filtered curvature. Plots show the decomposition of curvature at point (I) (II) or (III). CFP segmentation is presented for median size brain on a smoothed anatomy with a gyral mask (salmon red). TFP: total folding power.

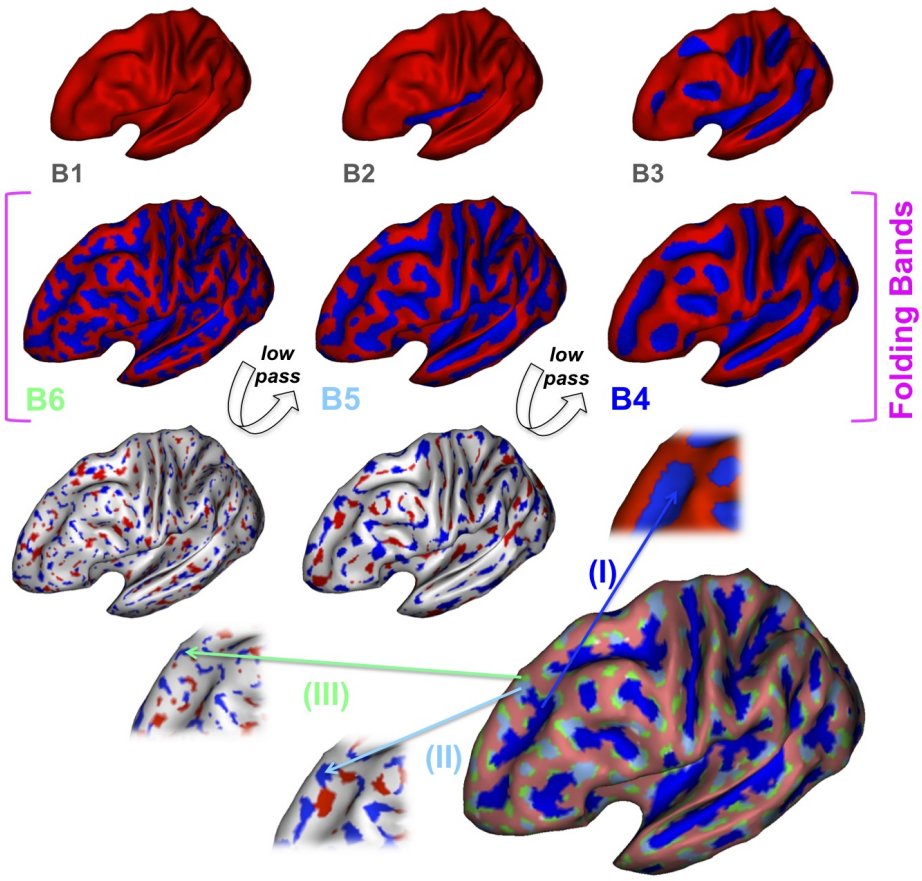

Fig 5: Segmentation of CFP according to the locally patterning band.

1st and 2nd row show the series of low-pass filtered cortical folding pattern. Local magnifications show the subtraction step between two consecutive levels in the neighborhood of points (I) and (II). CFP segmentation is presented for median size brain on a smoothed anatomy with a gyral mask (salmon red).

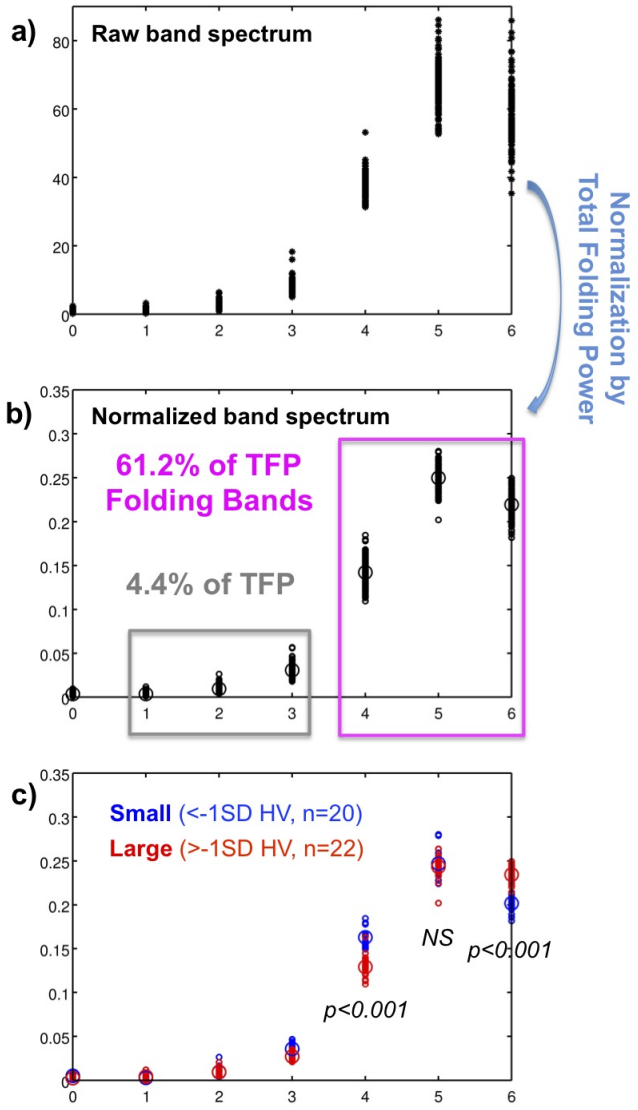

Fig 6: Spectral proportions.

a) Raw band spectrum for the whole dataset.
b) Normalized band spectrum i.e. spectral proportions for the whole dataset TFP: total folding power.
c) Differences of spectral proportions between small (HV below mean-1SD) and large (HV over mean+1SD) brains of the database. Student testing for mean differences. HV: hemispheric volume, NS: non significant.

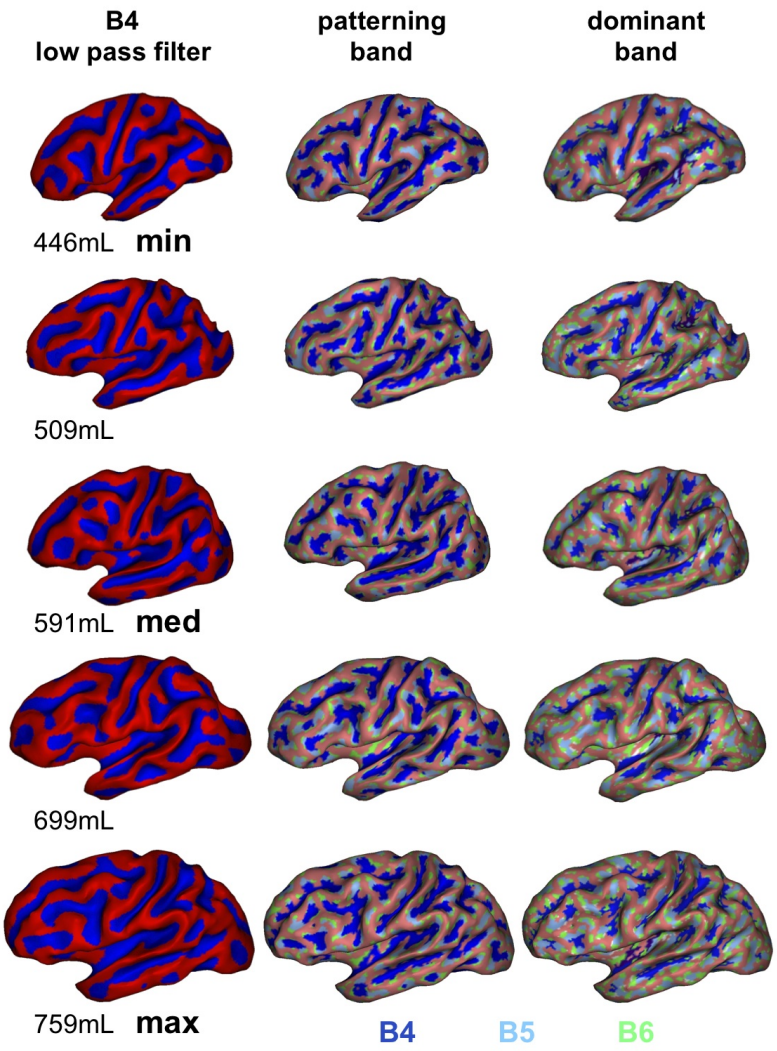

Fig 7: Spectral segmentation of CFP along dataset.

Brains of increasing size, measured by their hemispheric volume. 1st column: regular pattern of B4 low-pass filtered CFP. 2nd column: segmentation according to patterning band showing increase of B6 tagged ramifications with size. 3rd column: segmentation according to dominant band showing extension of B5 and B6 tagged surface. CFP segmentation is presented on a smoothed anatomy with a gyral mask (salmon red).

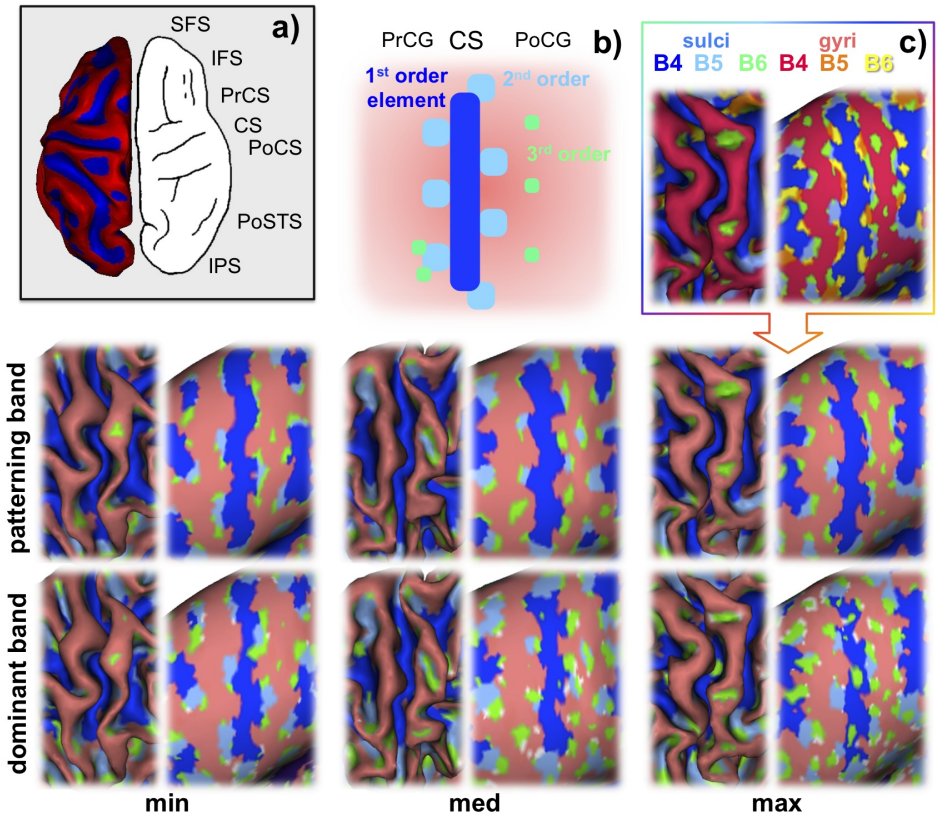

Fig 8: Anatomical- spectral correlations.

a) Primary folding fields corresponding to B4 low-pass filtered CFP. Comparison between regular pattern of B4 low-pass filtered CFP and primary folds described by (Chi et al., 1977) for left hemisphere. Primary folds appears before 32weeks of gestation. The schematic left hemisphere is adapted from (Chi et al., 1977) and switched to the right side. SFS: superior frontal sulcus, IFS: inferior frontal sulcus, PrCS: pre-central sulcus, CS: central sulcus, PoCS: post-central sulcus, PoSTS: posterior branch of the superior temporal sulcus, IPS: intra-parietal sulcus. b) Spectral segmentations of the central region: 1st 2nd and 3rd order elements of CFP.
Schematic interpretation of the segmentations is given in the 1st row. The number of 3rd order elements is arbitrary since it increases with brain size. For each brain, the segmentation is presented on the native (left) and totally smoothed (right) anatomy with a gyral mask (salmon red). min, med, max: brain of minimum, median and maximum size of the database.
c) Spectral segmentations of the central region for the whole CFP (without gyral masking).

a)

	B1		B2		B3		B4		B5		B6		resolution		HV (cm^3)	HA (mm^2)
	EV order	WL (mm)	EV order	WL (mm)	EV order	WL (mm)	EV order	WL (mm)	EV order	WL (mm)	EV order	WL (mm)	EV order	WL (mm)		
mean	2	447	6	212	21	110	78	56	296	28	1111	14	3832	7	591	77327
SD	0	24	0	12	1	6	4	3	12	2	41	1	142	0	50	7623
min	2	396	6	188	19	97	71	49	274	25	1036	12	3550	6	445	57323
median	2	445	6	211	21	110	78	56	295	28	1106	14	3823	7	591	72780
max	2	513	6	248	25	126	94	64	343	32	1267	16	4305	8	759	97199

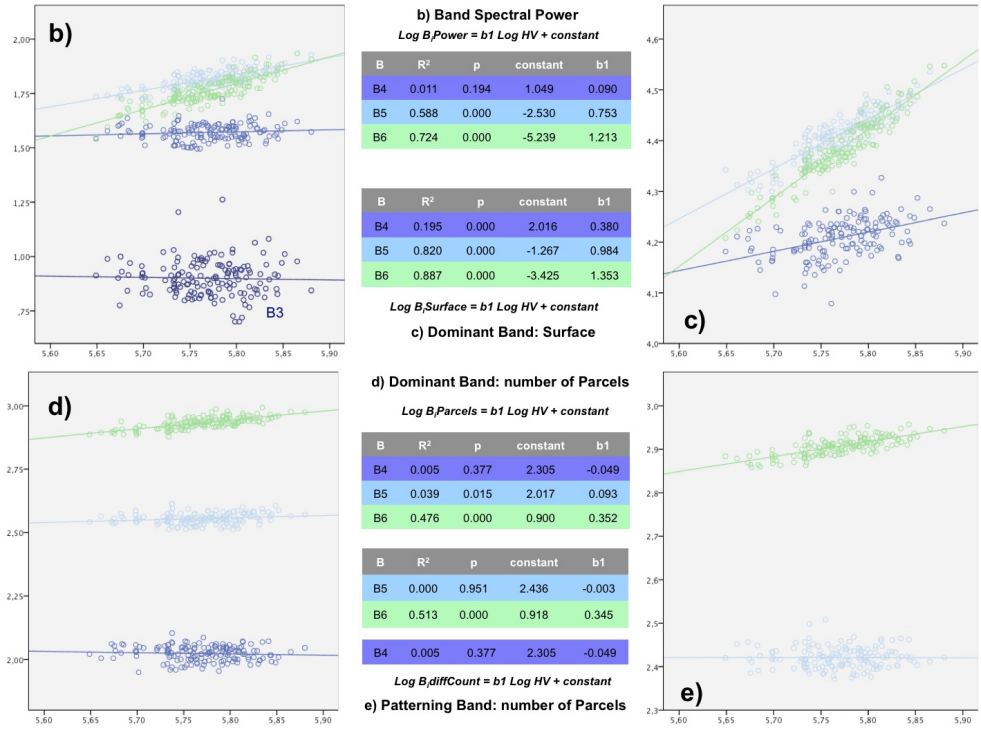

Fig 9: Allometric scaling for CFP extension.

a) Spectral sizing: bandwidth, resolution and brain size WL: wavelength, EV: eigenvalue/eigenfunction.
b) Band spectral power scaling. Isometry for B4, following global positive allometry for B5 (same scaling exponent than total folding power = 0.753), accentuated positive allometry for B6 (1.213).
c) Scaling of the surface of dominance for each band. Same behavior than band spectral power.
d) Scaling of the number of parcels of dominance for each band. The number is independent of size for B4 and B5 but increases for B6.
e) Scaling of the number of patterned parcels for each band. Same behavior than number of parcels of dominance.